JOURNAL OF AIRCRAFT
Vol. 37, No. 4, July–August 2000

# Experimental Geometry Optimization Techniques for Multi-Element Airfoils

Drew Landman* and Colin P. Britcher†
*Old Dominion University, Norfolk, Virginia 23529-0247*

**Experimental geometry optimization techniques for high-lift airfoils are reported. A modern three-element airfoil model with a remotely actuated flap was designed, tested, and used in low-speed wind-tunnel experiments to investigate optimum flap positioning based on lift. Detailed results for lift coefficient vs flap vertical and horizontal position are presented for two airfoil angles of attack, 8 and 14 deg. Two automated optimization simulations, the method of steepest ascent and a sequential simplex method, were demonstrated using experimental data. A simple online optimizer was successfully demonstrated with the wind-tunnel model that automatically seeks the optimum lift as a function of flap position. Hysteresis in lift as a function of flap position was discovered when tests were conducted using continuous flow conditions.**

## Nomenclature

$C_l$ = lift coefficient, $L/qc$
$C_{l\max}$ = maximum lift coefficient
$C_p$ = pressure coefficient, $(P - P_\infty)/q_\infty$
$c$ = airfoil nested chord length
$L$ = lift
$N$ = number of iterations
$P$ = local static pressure
$P_\infty$ = freestream static pressure
$q$ = dynamic pressure
$Rec$ = chord Reynolds number, $\rho V c/\mu$
$V$ = velocity
$y$ = vertical spatial coordinate
$\alpha$ = angle of attack (referenced from nested airfoil max length line)
$\delta_{\text{flap}}$ = flap deflection angle
$\delta_{\text{slat}}$ = slat deflection angle
$\mu$ = viscosity
$\rho$ = density
$\%c$ = percent of nested chord length

## Introduction

AN important practical problem in wind-tunnel testing of multi-element airfoils is the requirement to test a range of configurations to ensure that the optimum is chosen. Unfortunately, this is very time consuming if one considers all of the variables such as flap position and deflection, slat position and deflection, angle of attack, Mach number, and Reynolds number. Nomenclature for multi-element airfoils is reviewed in Fig. 1. The majority of tunnel occupancy (time) may be expended during traditional model geometry changes that necessitate lengthy delays in testing as the relative position of elements is manually set and measured. To optimize a high-lift geometry, tests should be conducted at near-flight Reynolds numbers, which severely limits the number of facilities suitable for high-lift testing.[1–4] The number of variables, the economics of tunnel occupancy, and the development time constraints realistically dictate the development of a sparse test matrix.

Although computational methods for multi-element airfoils have improved in recent years, the state of the art is still primarily limited to providing reliable lift predictions for two-dimensional configurations free of large areas of separation.[5] Computational fluid dynamics (CFD) results can at least be used to provide a starting point for choosing a range of gap and overhang settings.[3,5] Recent studies illustrate the current methodology for identifying optimal rigging of multi-element airfoils using wind-tunnel testing.[1,5–7] Individual element optimization is performed experimentally, whereas the other elements remain in a conservative setting, meaning a choice of gap and overhang (OH) that, based on experience, is thought to provide adequate slot flow without risking separation. This is followed by complete system optimization to find the highest performance possible. A relevant example is an optimization study performed in the NASA Langley Research Center low-turbulence pressure tunnel (LTPT).[7] The study focused on obtaining maximum lift coefficients for two advanced subsonic transport high-lift landing configurations, the first a three-element and the second a four-element configuration. The optimal gap and OH settings were shown to be both Reynolds number and Mach number dependent, and so a flight condition representative of the stall-critical section of the wing was chosen for geometry optimization. Flap deflection was fixed and a conservative gap and OH chosen. A slat optimization was next performed using three slat deflection angles and a total of 17 gap and OH settings. A single-element flap optimization was performed last with the use of two deflection angles and a total of 15 gap and OH settings.

## Motivation and Scope of the Present Work

The current practice of adjusting element rigging manually has been shown to be the most time-consuming component of a multi-element airfoil wind-tunnel optimization study. The present work seeks to demonstrate the practicality of automated experimental optimization of multi-element airfoils. A modern two-dimensional, three-element airfoil with internal flap actuators was used to explore the possibility of in situ optimization of flap position for best lift. The work presented represents a first step toward developing an automated, fully three-dimensional modeling approach to multi-element airfoil optimization at near-flight conditions.

This paper should interest researchers for two reasons: 1) Lift coefficient distributions are presented for a broad range of flap gap and OH riggings for two angles of attack measured using the servo-actuated flap. 2) The viability of a simple online optimizer, seeking best lift coefficient by varying the position of the flap was successfully demonstrated for four different configurations.

## Actuators for Two-Dimensional Multi-Element Airfoil Testing

When faced with the prospect of designing a remotely actuated two-dimensional high-lift airfoil model, the designer will typically

Received 27 April 1999; revision received 24 February 2000; accepted for publication 1 March 2000. 

*Assistant Professor, Department of Aerospace Engineering. Member AIAA.
†Associate Professor, Department of Aerospace Engineering. Senior Member AIAA.

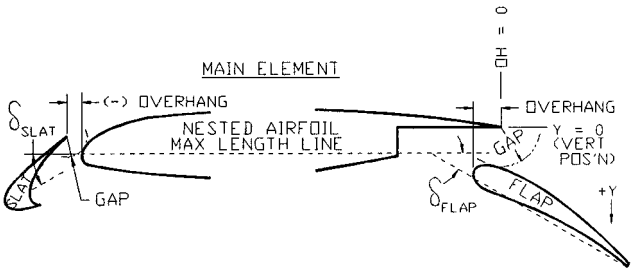


**Fig. 1 Multi-element airfoil nomenclature.**

have two choices: use internally mounted actuators or build actuators into the tunnel sidewall. When the designer concentrates on flap actuation, the internal design requires flap brackets to connect the flap to drive stages buried in the main element. The intrusion of brackets into the flowfield is a disadvantage, but they can be placed in such a way as to minimize spanwise flap deflection under load. The available space in the main element can be limiting and certainly requires the use of complex miniature components such as servomotors, gear trains, and linear bearings. The load capacity of internal actuators will tend to be inferior to sidewall mounted counterparts due to space constraints. Two advantages of this approach are the portability of the model and the ease of installation in multiple facilities.

The sidewall configuration allows the flap to be end mounted and driven through the wall. The greatest advantage to this approach is the larger space available for high-powered actuators. The advantage of the lack of flap-bracket generated flow interference is offset by the disadvantage of a more flexible mounting, which causes increased spanwise deflection of the flap. The flap acts as a prismatic beam under the influence of a uniformly distributed load. If the flap is simply supported, the deflection is excessive and greatest at midspan. Conversely, if the ends of the flap are preloaded with restoring moments, the midspan deflection can be adjusted to zero.[8]

These two design approaches were compared by calculating the flap deflection under load for a typical example. It is shown easily that the maximum flap deflection over the central portion of the model's span is lower when the flap is supported by brackets located one-quarter span from each end, compared to a sidewall-supported case with imposed end moments.

Internal actuators were chosen for this study for two reasons. It was felt that the greatest advantage to this concept was the portability of the model. In the planning stages, several wind tunnels were chosen as possible candidates for the study, hence, our building a specialized sidewall actuation system was impractical. In addition, because this investigation was treated as a proof-of-concept endeavor, low-speed wind tunnels were chosen as the target test facilities and the lower air loads permitted the use of the less powerful internal actuator concept.

## Experimental Details

### Wind-Tunnel Model

A unique model with internal actuators was specially designed using an airfoil geometry representative of a modern civil transport. The coordinates are considered proprietary but have been used for computational and experimental work as part of the CFD Challenge held at NASA Langley Research Center.[5] The three-element high-lift model, shown in Fig. 2, has a nested chord of 18 in. and a span of 36 in. All elements were numerically machined: the slat and main element from solid aluminum stock and the flap from stainless steel to ensure minimal deflection. All elements were designed with a seamless upper surface with chordwise pressure taps located midspan on the top and bottom surfaces. The slat was attached by four adjustable stainless steel brackets located on the underside of the main element. Slat deflection was fixed at 30 deg for the entire test; gap and OH were varied by installing shims under the brackets. The flap was designed for a positional gap range from 1.38 to 4.4%$c$ (based on the nested chord of the entire model) and an OH range

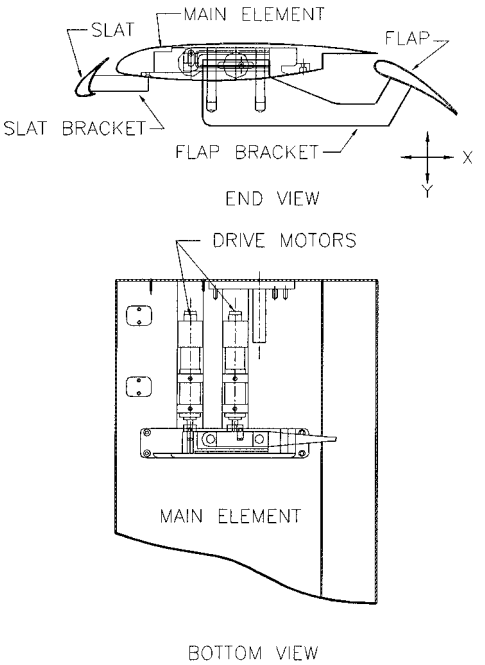


**Fig. 2 Three-element airfoil wind-tunnel model.**

from −1.38 to 3.63%$c$. The flap deflection angle was fixed at 30 deg for this study.

The flap is positioned using four servomotors located in the main element arranged in two-degree-of-freedom stages, two motors to a stage, as shown in Fig. 2. Each motor has an axially mounted eccentric cam and follower driven through a planetary gear drive. Linear motion is provided by a dovetail slide in the horizontal direction (chordwise) and parallel pins in the vertical direction. Flap brackets were located at a distance of one-quarter span from the tunnel walls and were designed for minimal deflection to maintain a constant gap and overhang. Flow interference was felt to be minimal and not a significant factor for this study.

### Wind Tunnel and Instrumentation

The Old Dominion University, Department of Aerospace Engineering, 4 × 3 ft low-speed wind tunnel was used to obtain all of the results presented. This wind tunnel is a closed return, fan driven, atmospheric pressure tunnel using a 125-hp electric motor to provide speeds in excess of 120 mph. The test section is 4 × 3 ft in cross section and 8 ft long. The freestream turbulence intensity in this facility does not exceed 0.2% (Ref. 9).

The model was mounted vertically spanning the 3-ft dimension. Flap ends were sealed to the tunnel wall using overlapping movable panels. Angle of attack was set by rotating a plate in the tunnel floor. Wind-tunnel dynamic pressure was determined based on the pressure differential across the contraction cone with an MKS 310 differential pressure transducer and MKS 170 amplifier. A Hewlett–Packard Company 3497A data acquisition and control unit with 6.5-digit accuracy was used to sample voltages. A National Aperture MC-3SA four-axis motor control unit and card were used to command the motors. Initially, pressures were measured using a bank of 12 Datametrics Barocells (10 torr) and later using Pressure Systems Incorporated (PSI) model 9010 (10 and 20 in. of water) electronically scanned pressure transducers.

### Flow Conditions

The maximum tunnel speed was constrained by the maximum aerodynamic loads the flap actuators could bear. The Reynolds number was $10^6$ based on the nested chord for the entire study. Spanwise flow uniformity was evaluated in two ways. First, the model was fitted with minitufts and run through an angle-of-attack sweep at the design speed. Tufts were monitored for evidence of separation and

spanwise flow with particular attention to tufts near the wall–model interface.[10,11] Second, the spanwise pressure variation was monitored on the flap and main element through six spanwise taps located near the trailing edge of each element. The flow was considered two dimensional if the spanwise variation in pressure coefficient was less than 5% of the difference between the maximum and minimum value of the pressure coefficient for the entire airfoil.[10] No sidewall boundary-layer control was employed, but rather the maximum angle of attack was limited to 14 deg to maintain acceptably uniform flow across the span.[12]

All of the tests in this study were conducted with free boundary-layer transition, meaning there were no added tripping devices or surface roughness elements on the airfoil. In a related study using the same model, roughness elements were added to force transition on the upper surface of all of the elements. It was felt that the forced transition would eliminate the possibility of laminar separation bubble-induced hysteretic effects.[13,14] Forcing transition is one method for simulating higher Reynolds number flows, which has the benefit of allowing comparisons to higher Reynolds number data.[15,16] A number 30 grit abrasive particle was chosen as the minimum size roughness element necessary to assure transition.[17] The particles were distributed over an approximately 0.2-in.-wide strip at the 5% element chord location on the top surface of each element.[15,18] Comparison of baseline lift distributions (vs flap position) between the free and forced transition measurements revealed only slight differences that were on the order of the measured uncertainty.

## Baseline Results

All results are presented without corrections for boundary effects. The slat and flap deflection was fixed at 30 deg. Two slat settings were used; setting A had a 3.03%$c$ gap and a $-2.46\%c$ OH, and setting B used a 2.17%$c$ gap and a $-1.46\%c$ OH.

### Comparisons to Reference Data

A larger model using the identical geometry was tested in the LTPT at NASA Langley Research Center in conjunction with the aforementioned CFD Challenge.[5] Force and moment data and pressure distributions from these tests have been published in recent literature at two Reynolds numbers: $5 \times 10^6$ and $9 \times 10^6$, where the latter value is representative of a flight Reynolds number for a narrow-body transport.[5] Figure 3 shows the correlation of lift data from this study to the data from the LTPT; both data sets are uncorrected for boundary effects. Lift coefficient from the LTPT study is plotted as a function of Reynolds number and angle of attack for an approximate overhang value of 0.078%$c$ and an approximate vertical position of 1.512%$c$. The Reynolds number scaling was

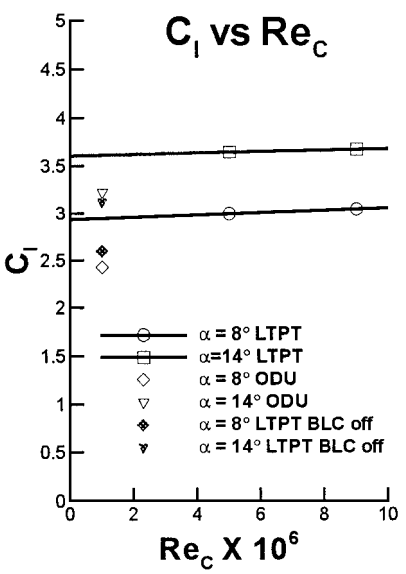


**Fig. 3 Comparison to reference lift data.**

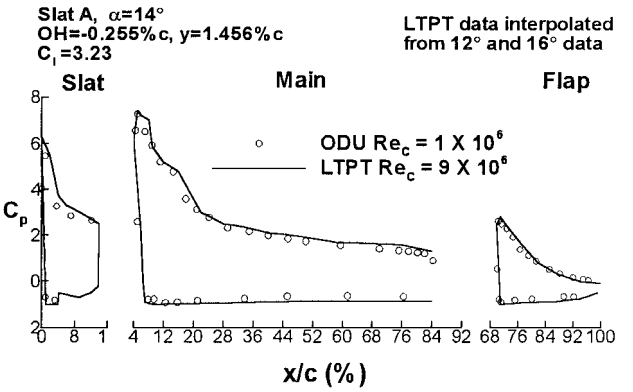


**Fig. 4 Comparison to reference pressure distribution.**

obtained from the linear fit shown. The boundary-layer control correction was made using representative data presented by Paschal et al.[12] A comparative pressure distribution is presented in Fig. 4 using a flap rigging that is extremely close to the LTPT data.

The lower values for lift coefficient for the current study are attributed to the lack of sidewall boundary-layer control,[12] small differences in gap and OH, the reduced number of pressure taps, and the lower Reynolds number of the test condition. The key features of the reference pressure distribution appear to be captured by the less densely tapped surfaces of the model from this study. In particular, the inflection point on the upper surface of the main element ($x/c \sim 15\%$) and the suction peak on the main element and flap are well represented. The sparse tap distribution on the slat somewhat reduces the detail but was found to be adequate for resolving small changes in overall airfoil lift coefficient.

The remotely actuated flap was used to vary flap gap and OH both with the tunnel flow on continuously and with the flow restarted between successive data points (hereafter called intermittently). In both cases, for fixed slat riggings, excessive flap gap settings led to separation on the flap progressing from the trailing edge and moving forward as the gap was increased. This separation trend was identified by the constant pressure region at the trailing-edge flap and verified using tufts.[19,20] The nature of the progression of flap stall was found to be both path dependent and dependent on whether the tunnel was operated continuously or intermittently. Lift hysteresis due to flap position was found to exist when lift coefficients were evaluated using continuous flow conditions, hampering the use of simple optimizing methods. The data presented in this paper were obtained using only intermittent conditions. However, the lift hysteresis phenomenon was studied in detail and will be the subject of a future publication.

### Lift Coefficient vs Flap Position

In the interest of investigating the feasibility of on-line automatic optimization of the airfoil lift coefficient, test runs were initiated to measure lift coefficient over the available flap positional range to serve as a baseline. Two angles of attack were chosen as relevant: 8 deg, representative of an approach angle of attack, and 14 deg, the highest angle of attack with acceptable spanwise flow uniformity.

Baseline lift distributions were compiled using the A and B slat setting for the 8-deg case using 44 and 48 data points per plot, respectively (each point is the airfoil lift coefficient computed using the integrated pressure data). Representative results are shown in Fig. 5 and reveal a broad optimum region. When comparing slat settings, this region is located in approximately the same area, appears to be insensitive to slat setting, and is adequately represented by the number of points chosen. The steep gradient occurs where the flow separates from the upper surface of the flap. The lift coefficient distribution of the 14-deg case revealed a more definitive optimal region, characterized by two local maxima, one located at a 2%$c$ vertical position and 1%$c$ OH, the second near the extreme limits of vertical positioning and a 0.25%$c$ OH position. Figure 6 shows the results using 40 points with slat A. It was felt that more detail may

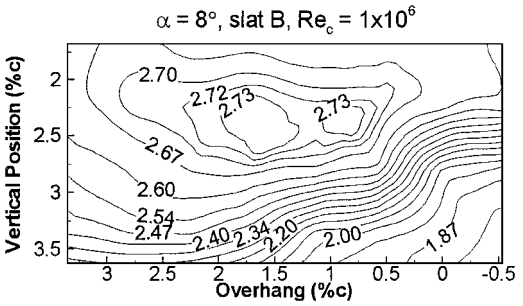


**Fig. 5 Lift coefficient vs flap position, representative baseline for $\alpha$ = 8 deg.**

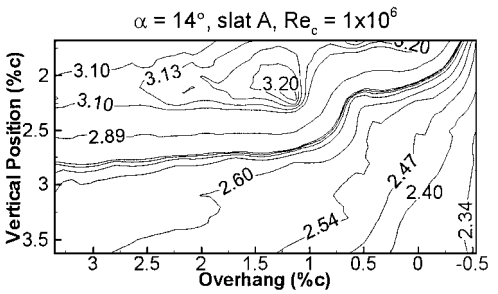


**Fig. 6 Lift coefficient vs flap position, representative baseline for $\alpha$ = 14 deg.**

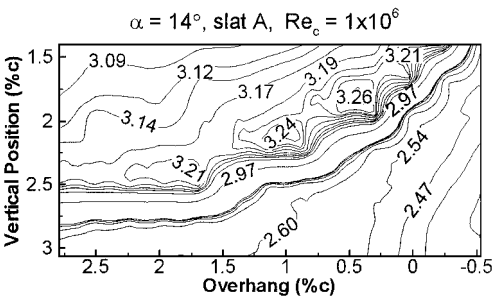


**Fig. 7 Lift coefficient vs flap position, dense grid, representative baseline.**

be present than the coarse grid size revealed, and the tests were run again with 120 points, omitting the region below 3%$c$ in the vertical direction where flow over the flap was separated. The resulting lift distribution using slat A is shown in Fig. 7. When we compare slat settings, the lift distributions were characterized by a greater sensitivity to the slat setting than the 8-deg case. For instance, $C_{l\,\max}$ for the B setting was 4% higher. The local maximum visible at the extreme vertical position appears to be a very small region and corresponds to the optimum position for $C_{l\,\max}$ chosen by Lynch for this airfoil geometry.[1]

#### Uncertainty Assessment

Having found the baseline lift distributions, the next tests were aimed at quantifying the uncertainty in lift coefficient due to the collective error of instrumentation, positioning hardware, and data-reduction algorithms. Two tests were devised. The first used a positioning program to twice sample a grid of 29 different points for an 8-deg angle of attack using slat A and restarting the tunnel after every point. The discrepancy in $C_l$ between the runs averaged 0.71% with a standard deviation of 0.75%. The second test set the angle of attack at 14 deg using slat B. Two points were chosen: a point where the flow over the flap upper surface was fully separated and a point where flap gap and OH were near optimal settings. Each point was evaluated 30 times by first moving the flap to a reference point, then to the evaluation point, starting the tunnel, obtaining pressure data, then turning off the flow and repeating the sequence. The standard deviations of $C_l$ for the separated point and the attached point were found to be 0.16 and 0.36%, respectively. These tests showed that the uncertainty in $C_l$ was low enough to permit the use of simple optimization routines. The variation in the results between the cases of the second test were felt to be explained by at least two factors. First, fully separated flow on the flap generates more benign interactions with the tunnel sidewall boundary layer. The attached case tends to introduce unsteady three-dimensional effects (such as corner vortices) at or near the end regions of the flap, whose influence may be felt at the midspan pressure tap locations. Second, the integration of the pressures over the sparsely tapped slat may introduce error if a sharp suction peak lies alternately coincident with, then adjacent to, a tap location.

## Optimization for Maximum Lift Coefficient

#### Simulation

The baseline lift coefficient distributions provide a database for use in a simulated experiment where the optimization problem is defined by the objective function $C_l = C_l(\mathrm{OH}, y)$. The two design variables OH and $y$ are the spatial coordinates defining the flap position. There are no constraints imposed on the problem as the limits of travel afforded by the wind-tunnel model design provided a range of motion that exceeded the design space. By using a multivariate regression, a response surface was generated using the discrete points of the baseline studies. This response surface, an example of which is shown in Fig. 8, now serves as a simulated experiment by adding simulated experimental uncertainty (noise equivalent to a standard deviation in $C_l$ of 0.017) (Ref. 8). The problem now was to maximize the response and airfoil lift coefficient for the design variables OH and $y$, the horizontal and vertical flap position variables. The choice of optimizers was based on the low noise level in the response and a desire to maintain a simplified approach in this feasibility study. The method of steepest ascent, a gradient method, was chosen first for its simplicity.[21,22] The second choice was the variable size sequential simplex method, a search method based on an adaptively sized geometric figure (a triangle for two design variables), chosen for its simplicity, robustness, and freedom from evaluations of derivatives of the objective function.[23,24] The details of both methods are omitted here, and the reader is guided to the Refs. 21, 22, and 24 for completeness. In addition, a fixed-size sequential simplex method was evaluated but quickly abandoned in favor of the variable size method.[8]

#### Results from the Optimizer Simulations

To evaluate the optimizers for use with an online experiment, experiment simulations were carried out with data from the 8- and 14-deg angle-of-attack baseline studies using slat settings B and A, respectively. It was found that the scaling parameters in the method of steepest ascent could be adjusted to provide rapid convergence for both sets of experimental data. This was considered a real advantage over the simplex method, which required separate adjustments of

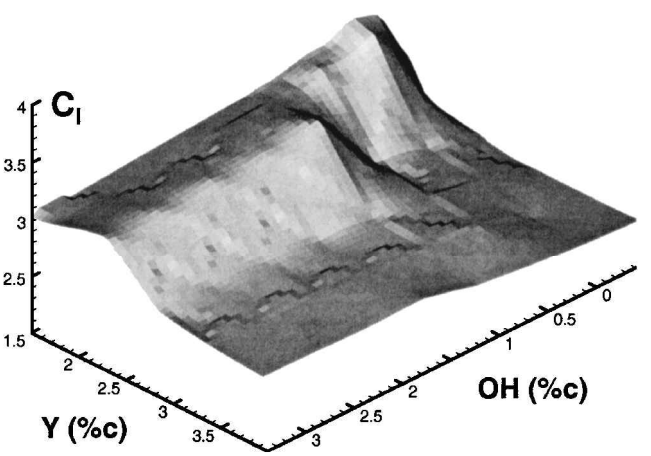


**Fig. 8 Response surface, $C_l = C_l(\mathrm{OH}, y)$.**

**Table 1 Comparison of simulation results: variable size simplex vs steepest ascent[a]**

| | $\alpha = 14$ | | $\alpha = 8$ | |
|---|---|---|---|---|
| Overhang | OH = 0.578%$c$ | OH = 2.245%$c$ | OH = 0.578%$c$ | OH = 2.245%$c$ |
| Steepest ascent | | | | |
| Average % difference of $C_l$ | 0.361 | 0.644 | 0.67 | 0.667 |
| Average standard deviation of $C_l$ | 0.015 | 0.02 | 0.02 | 0.018 |
| Sequential simplex | | | | |
| Average % difference of mean $C_l$ | 0.406 | 0.692 | 0.598 | 0.403 |
| Standard deviation of mean $C_l$ | 0.016 | 0.029 | 0.009 | 0.012 |

[a]Vertical flap position $y = 2.789\%c$.

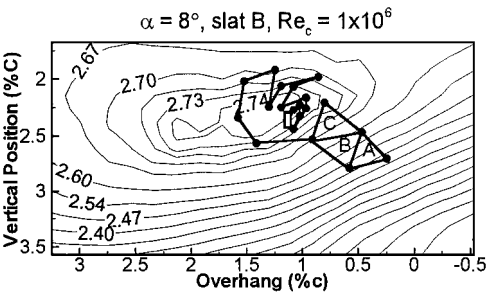


**Fig. 9 Example of sequential simplex simulation.**

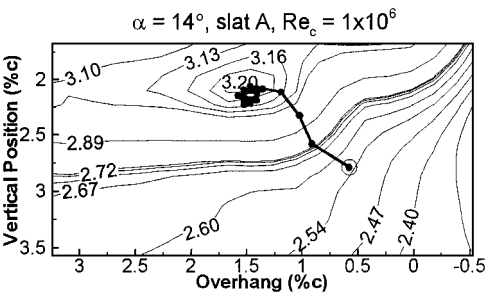


**Fig. 10 Example of steepest ascent simulation.**

scaling parameters for the two cases. If blind optimization was to be attempted, the more flexible method of steepest ascent was preferable. To compare the convergence characteristics of the methods, four trials were conducted using 30 runs for each method for each of two starting points. The optimizer paths were always begun in a portion of the design space where the flow over the flap upper surface was fully separated. Two start points were chosen to compare the methods: an aft point at OH $= 0.578\%c$, and $y = 2.789\%c$, and a forward point of OH $= 2.245\%c$, and $y = 2.789\%c$. The steepest ascent optimizer was run for 27 steps, the number of simplexes used in a run. Convergence was judged by examining the difference between the global optimum and the final run value of $C_l$. This method of comparison favored the simplex method, which was found to converge at a slower rate but often more fully than the ascent method. The ascent method, on the other hand, would most often converge to its final value in three to four steps. Table 1 provides a compilation of comparative results from the 30 runs of each trial.

Examples of a simplex simulation are shown in Fig. 9 and a steepest ascent simulation is shown in Fig. 10. In Figs. 9 and 10, the response surface, derived from the multivariate fit of data from the baseline study, is plotted under the optimizer path. The initial simplex is shown with the letter A and progresses alphabetically to the final simplex that lies within the rectangular border. The start point of the steepest ascent path is circled and the final point is denoted by the open oval inside the cluster of points near the optimum. Although both methods were clearly candidates for use as an online experimental optimizer, the steepest ascent method was ultimately chosen.

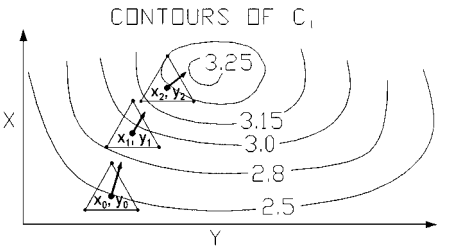


**Fig. 11 Method of steepest ascent.**

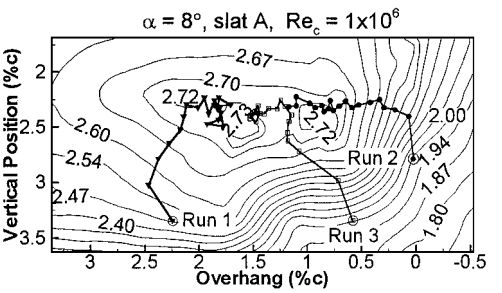


**Fig. 12 Results from experimental flap optimization, $\alpha = 8$ deg, slat A.**

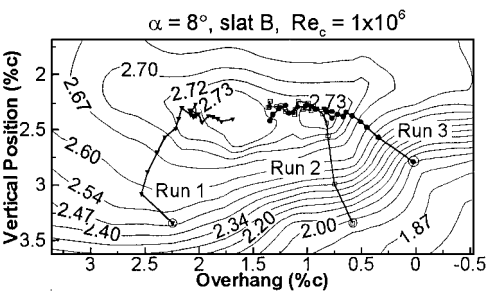


**Fig. 13 Results from experimental flap optimization, $\alpha = 8$ deg, slat B.**

**Experimental Optimization: Method of Steepest Ascent**

With the use of the algorithm for the method of steepest ascent (shown schematically in Fig. 11) with scaling values chosen during the simulation, a LabVIEW™ program was written to automatically seek the flap position that provided the maximum lift. This program starts with an arbitrary point, computes the gradient of the lift coefficient, and uses the ratio of successive gradient magnitudes in a scaling function to determine the next step size.[8] Lift coefficients used for the gradient computation are measured at each vertex of an equilateral triangle (side length $0.0033\%c$) about the centroid of the current evaluation point. The planar surface defined by the three points is used as an approximation for the local response surface and serves as an analytical model for computation of the gradient. An optimizing run began by input of the desired start point and ended when the chosen number of steps had occurred.

Two trials of three runs each were conducted using an angle of attack of 8 deg and the A and B slat settings. The six runs are shown in Figs. 12 and 13 where the start point for each run is circled. A

representative convergence history from Fig. 12 is plotted in Fig. 14. All runs in this trial were felt to be successful.

Seven runs, shown in Figs. 15 and 16, that demonstrate the viability of the optimization routine were recorded for the 14-deg case. In the first run of Fig. 15, the path can be seen to ridge walk where the path zigzags across the optimal region, often found when using the method of steepest ascent.[22] Run 2 was cut short by an equipment failure and was repeated as run 3. Note that the path of run 3 is nearly identical to run 2 over the first four points, and then begins to move on into the optimum region. Figure 16 illustrates more ridge walking where the path of run 2 quickly moves directly to a maximum and then walks back and forth over the ridge. In Figs. 15 and 16 the paths of the more forward start points appear to be ridge walking slightly out of the baseline plateau where the flow over the flap is attached. Reviewing the convergence history of Fig. 15, Fig. 17 shows that none of the $C_l$ values coincide with values for a region of fully separated flow over the flap. This phenomena is thought to be due to small changes in angle of attack between the baseline wind-tunnel entry and the optimizer entry, as well as the possibility that the baseline grid may not capture the exact location of the onset of separation. Slightly higher values of $C_l$ between baseline and optimizer data for identical flap positions are also accounted for by the dual entries.

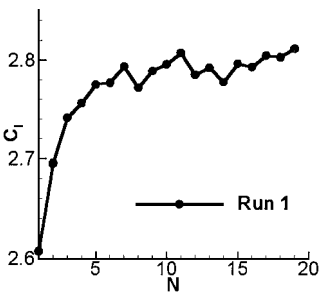


**Fig. 14 Sample convergence history from Fig. 12.**

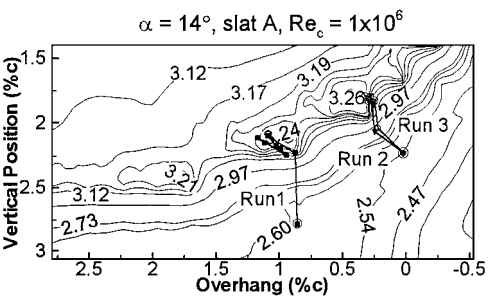


**Fig. 15 Results from experimental flap optimization, $\alpha$ = 14 deg, slat A.**

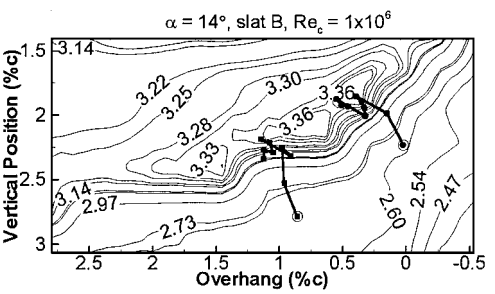


**Fig. 16 Results from experimental flap optimization, $\alpha$ = 14 deg, slat B.**

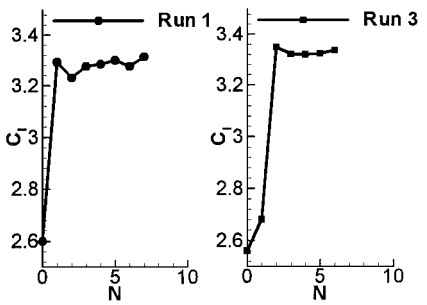


**Fig. 17 Sample convergence histories from Fig. 15.**

No convergence criteria were invoked in the optimizer routine in the interest of exploring the effects of noise in the optimal region. For example, premature indication of convergence would have terminated lengthy wind-tunnel runs, requiring restarts. The number of steps chosen was based on the length of a practical run (3 h for 20 points using PSI transducers). A convergence criteria is clearly viable. For instance, if for a given number of steps (for example, four) the lift coefficient remains within a tolerance (for example, ±0.01), the run is stopped. If this criteria is applied to the data of Fig. 14, the runs would have been stopped after 14–15 steps. Alternately, the criteria could be based on flap position.

### Extension to Three-Dimensional Testing

Internal flap actuators, located inside the main element of a two-dimensional model have been demonstrated to work well with the loads associated with a low Mach and low Reynolds number flow condition. There is an opportunity to extend this technology directly to three-dimensional models under similar flow conditions; however, it is ineffective to optimize element gap and OH at conditions that are vastly lower in Reynolds and Mach number than flight conditions.[1,3,6]

Unfortunately, lift loads at near-flight conditions are extremely high, which causes leading-edge and trailing-edge elements to deflect and challenges the model designer to create a powerful actuator that is compact enough to reside in the wing. For comparison purposes, consider the maximum lift force generated by a representative two-dimensional, three-element, high-lift airfoil at the conditions of the current study ($Re_c = 1 \times 10^6$) vs flight conditions ($Re_c = 9 \times 10^6$). Choosing a representative $C_{l\,\max} \sim 4.5$ and a chord of 0.5 m, the maximum lift per unit span is approximately 3750 N/m for $Re_c = 1 \times 10^6$ and 303,750 N/m for $Re_c = 9 \times 10^6$. At the present time, the limited size of facilities capable of these conditions and the extreme loading may suggest the need for semi-span wing models. With minimal additional flow interference a third degree of freedom could be added, providing adjustable flap deflection. Multiple sets of flaps, that is, inboard and outboard, common to subsonic transport aircraft, further complicate automated model design.

The steepest ascent optimizer presented in this work is equally valid for both two-dimensional and three-dimensional testing. The objective function for a three-dimensional test remains the lift coefficient, albeit for the full wing. Additional degrees of freedom such as flap deflection angle can be incorporated readily into the gradient-based optimizer algorithm. A full three-dimensional program could also include optimization based on drag or lift-to-drag ratio. Model installations on sensitive force balances (vs integrated pressures) would provide the most convenient method for evaluating these quantities.

## Conclusions

This study served as a foundation on which further improvements in automated high-lift wind-tunnel model geometry optimization techniques can evolve. In situ geometry optimization of automated multi-element airfoils has been shown to be practical. Through the use of these techniques, large wind-tunnel productivity gains are realizable. In addition, a larger data set is typically made available for a given entry. The natural extension is to now develop a three-dimensional testing pilot study at near-flight conditions.

In our study of optimization techniques, lift hysteresis as a function of flap position was discovered using continuous flow-on conditions. When optimizing a high-lift system for best lift with a given flap rigging, the design variables may need to include the path traversed during flap deployment, as well as the gap, OH, and deflection.

## Acknowledgments

This work was partially funded by two American Society for Engineering Education summer faculty fellowships at the NASA Langley Research Center with the Experimental Flow Physics Branch (EFPB) (now the Flow Modeling and Control Branch) and the Subsonic Aerodynamics Branch. Additional funding was received from NASA Langley Rsearch Center task orders, one from EFPB and a second from the Multi-Disciplinary Design and Optimization Branch. Specifically, the authors wish to acknowledge the help of S. Robinson, M. Walsh, J. Lin, S. Klausmeyer, E. Waggoner, H. Morgan, J. Otto, and T. Zang.

## References

[1]Nelson, R. C., "An Overview of High-Lift Aerodynamics," AIAA Professional Studies Series, AIAA, Washington, DC, 1995.

[2]Butter, D. J., "Recent Progress on Development and Understanding of High Lift Systems," CP-365, AGARD, 1984.

[3]Lynch, F. T., "Experimental Necessities for Subsonic Transport Configuration Development," AIAA Paper 92-0158, Jan. 1992.

[4]Valarezo, W. O., Dominik, C. J., and McGhee, R. J., "Multi-Element Airfoil Performance Due to Reynolds and Mach Number Variations," *Journal of Aircraft*, Vol. 30, No. 5, 1993, pp. 689–694.

[5]Klausmeyer, S. M., and Lin, J. C., "Comparative Results from a CFD Challenge over a 2D Three-Element High Lift Airfoil," NASA TM-112858, May 1997.

[6]Lin, J. C., and Dominik, C. J., "Optimization of an Advanced Design Three Element Airfoil at High Reynolds Numbers," AIAA Paper 95-1858, 1995.

[7]Valarezo, W. O., Dominik, C. J., McGhee, R. J., Goodman, W. L., and Paschal, K. B., "Multi-Element Airfoil Optimization for Maximum Lift at High Reynolds Numbers," TP Vol. II, AIAA 9th Applied Aerodynamics Conf., AIAA Paper 91-3332, 1991.

[8]Landman, D., "Experimental Geometry Optimization Techniques for Multi-Element Airfoils," Ph.D. Dissertation, Dept. of Aerospace Engineering, Old Dominion Univ., Norfolk, VA, May 1998.

[9]Alcorn, C. W., "Boundary Layer Influences on the Subsonic Near-Wake of a Family of Three-Dimensional Bluff Bodies," Ph.D. Dissertation, Dept. of Mechanical Engineering and Mechanics, Old Dominion Univ., Norfolk, VA, Aug. 1993.

[10]Nakayama, A., Kreplin, H. P., and Morgan, H. L., "Experimental Investigation of Flowfield About a Multielement Airfoil," *AIAA Journal*, Vol. 28, No. 1, 1990, pp. 14–21.

[11]Morgan, H. L., Ferris, J. C., and McGhee, R. J., "A Study of High-Lift Airfoils at High Reynolds Numbers in the Langley Low Turbulence Pressure Tunnel," NASA TM-89125, July 1987.

[12]Paschal, K., Goodman, W., McGhee, R., Walker, B., and Wilcox, P. A., "Evaluation of Tunnel Sidewall Boundary-Layer-Control Systems for High-Lift Airfoil Testing," AIAA Paper 91-3243, 1991.

[13]Mueller, T. J., and Batill, S. M., "Experimental Studies of Separation on a Two-Dimensional Airfoil at Low Reynolds Numbers," *AIAA Journal*, Vol. 20, No. 4, 1982, pp. 457–463.

[14]Selig, M. S., Guglielmo, J. J., Broeren, A. P., and Giguère, P., "Experiments on Airfoils at Low Reynolds Numbers," AIAA Paper 96-0062, 1996.

[15]Barlow, J. B., Rae, W. H., and Pope, A., *Low Speed Wind Tunnel Testing*, 3rd ed., Wiley, New York, 1999, pp. 301–313.

[16]Pankhurst, R. C., and Holder, D. W., *Wind Tunnel Technique*, revised ed., Sir Issac Pitman and Sons, London, 1965.

[17]Braslow, A. E., and Knox, E. C., "Simplified Method for Determination of Critical Height of Distributed Roughness Particles for Boundary-Layer Transition at Mach Numbers from 0 to 5," NACA TN-4363, Sept. 1958.

[18]Papadakis, M., Myose, R. Y., and Matallana, S., "Experimental Investigation of Gurney Flaps on a Two Element General Aviation Airfoil," AIAA Paper 97-0728, 1997.

[19]Adair, D., and Horne, W. C., "Characteristics of Merging Shear Layers and Turbulent Wakes of a Multi-Element Airfoil," NASA TM-100053, Feb. 1988.

[20]Biber, K., and Zumwalt, G. W., "Hysteresis Effects on Wind-Tunnel Measurements of a Two-Element Airfoil," *AIAA Journal*, Vol. 31, No. 2, 1993, pp. 326–330.

[21]Fox, R. L., *Optimization Methods for Engineering Design*, Addison Wesley Longman, Reading, MA, 1971, pp. 71–78.

[22]Beveridge, S. G. G., and Schechter, R. S., *Optimization: Theory and Practice*, McGraw–Hill, New York, 1970, pp. 407–420.

[23]Spendley, W., Hext, G. R., and Himsworth, F. R., "Sequential Application of Simplex Designs in Optimisation and Evolutionary Operation," *Technometrics*, Vol. 4, No. 4, 1962, pp. 441–461.

[24]Walters, F. H., Parker, L. R., Jr., Morgan, S. L., and Deming, S. L., *Sequential Simplex Optimization*, CRC Press, Boca Raton, FL, 1991, pp. 76–158.